energy&fuels

Article

Cite This: Energy Fuels 2017, 31, 11225-11233

pubs.acs.org/EF

Zeolite-Supported Iron Oxides as Durable and Selective Oxygen Carriers for Chemical Looping Combustion

Lu Liu,[†,‡] Yiqing Wu,[†,§] Junkai Hu,[‡] Dongxia Liu,[*,§] and Michael R. Zachariah[*,‡,§]

[‡]Department of Chemistry and Biochemistry and [§]Department of Chemical and Biomolecular Engineering, University of Maryland, College Park, Maryland 20742, United States

Supporting Information

ABSTRACT: Chemical looping combustion (CLC) is a promising technology for fossil fuel combustion with inherent CO_2 separation from flue gases, circumventing high cost for CO_2 capture and NO_x elimination as in conventional combustion processes. Metal oxides are commonly used as oxygen carriers (OCs) in CLC. However, sintering and coking of OCs and the consequent degradation in their activity and durability during multiple cycles inhibit the practical applications of CLC technology. In the present study, we employed a silicalite-1 zeolite support to achieve OCs with high resistance against sintering and coking in CLC. Iron oxides (Fe_2O_3) with methane fuel were employed to demonstrate the approach and to quantify the influence of silicalite-1 support on conversion efficiency, durability, and selectivity of these OCs in CLC cycles. Two iron oxide−zeolite geometrical structures, a core−shell Fe_2O_3@silicalite-1 and a Fe_2O_3-impregnated silicalite-1 (Fe_2O_3/silicalite-1), were created to improve Fe_2O_3 stability. The CLC tests showed that both structures led to less aggregation of Fe_2O_3 OCs at 1223 K. A comparison between Fe_2O_3/silicalite-1 and Fe_2O_3@silicalite-1 in CLC tests illustrates that Fe_2O_3 impregnated in zeolite had higher durability than in the core−shell structure. The selectivity of CH_4 to CO_2 followed the order of Fe_2O_3/silicalite-1 > Fe_2O_3@silicalite-1 ≫ bare Fe_2O_3. The high selectivity of Fe_2O_3/silicalite-1 to CO_2 in CLC tests can be attributed to the encapsulation of Fe_2O_3 inside channels of silicalite-1 that provides physical barriers for aggregation of OCs in CLC cycles as well as coke deposition on OCs. In conclusion, our study of the structure−function relation for silicalite-1-supported Fe_2O_3 OCs can form the basis for the development of silicalite-1 as an efficient support in chemical looping applications.

1. INTRODUCTION

The capture of CO_2 released from fuel combustion is being actively studied to mitigate the effects of climate change.[1] A number of processes, such as pre-combustion,[2] oxy-fuel combustion,[3] and post-combustion,[4] have been explored for CO_2 capture from fossil fuel combustion processes. However, all of these techniques are energy-intensive, resulting in a decrease of the overall combustion efficiency.

Chemical looping combustion (CLC) is being explored as a next-generation combustion technology, because it operates with the same thermodynamic efficiency as air-based combustion but with a potential of near-zero CO_2 emission.[5] CLC involves a two-step process, in which metal oxides serve as the oxygen source rather than air, so that the direct contact between fuel and air is avoided. Hydrocarbon fuels are oxidized by metal oxides to water steam and CO_2 in the first step, from which a pure CO_2 stream could be realized by single-steam condensation.[6,7] The reduced metal oxide is then regenerated by combustion in air in the second step to complete the combustion cycle. The isolation of hydrocarbon fuels from air in CLC processes achieves a pure CO_2 steam for direct sequestration in an ideal situation and avoids NO_x formation by recovery of metal oxides at moderate temperature in air. Because of the multi-cycling nature of the process, the choice of metal oxides as oxygen carriers (OCs) with excellent activity and long-term stability is critical to enable implementation of CLC into industrial scale.[8]

Metal oxides based on copper, iron, nickel, manganese, etc. as well as their mixtures are the most promising OC candidates for CLC cycles because of their earth abundance, low cost, mechanical stability, and recyclability.[9−12] Among them, Fe-based OCs have received intensive research efforts because of their low cost, high melting point, and excellent mechanical strength at high temperatures.[13] The practical application of iron oxide OCs in CLC, however, has been impeded by serious sintering and a low reduction rate by fuels.[14−16] Eventually, the iron oxide OCs encounter agglomeration and deactivation and, thus, durability loss in multiple CLC cycles. The introduction of support materials for iron oxide OCs is being studied to conquer the durability and deactivation issues in CLC cycles. Currently, inert supports, including Al_2O_3,[17] SiO_2,[18] $MgAl_2O_4$,[19] TiO_2,[20] ZrO_2,[21] and CeO_2,[22] and active supports, such as perovskites,[23] have been considered for Fe_2O_3 OCs. The support materials help to promote dispersion of OC particles and provide physical/chemical barriers against OC migration into aggregates.[14,17−20] Moreover, the support can influence the oxide anion diffusion in the OC component, which facilitates the reaction rate of OCs in fuel combustion in CLC tests.[20] It should be noted that all of these support materials are oxides and their mixtures.

In the present work, we report a new type of support, a silicalite-1 zeolite, for Fe_2O_3 OCs in CLC. Silicalite-1 is the aluminum-free form of zeolite, with a mordenite framework inverted (MFI) structure consisting of two intersected 10

Received: June 13, 2017
Revised: August 30, 2017
Published: September 14, 2017

DOI: 10.1021/acs.energyfuels.7b01689
Energy Fuels 2017, 31, 11225−11233

Scheme 1. Synthesis Procedure To Prepare Fe_2O_3@Silicalite-1 OC

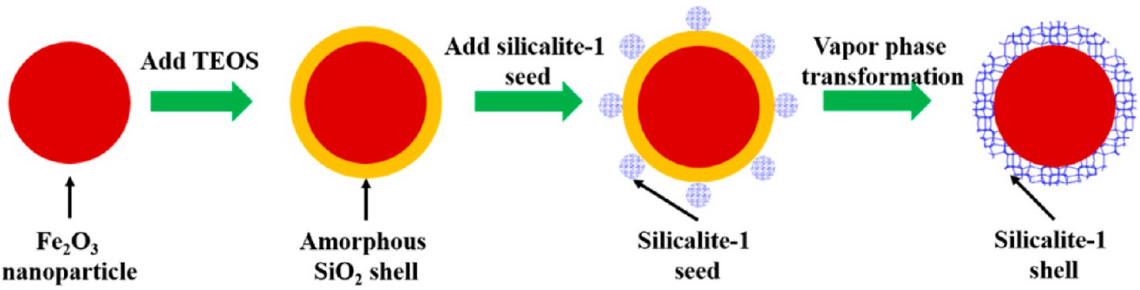

member ring (MR) microporous channels, one straight and one sinusoidal, with a diameter of ~0.55 nm.[24,25] Silicalite-1 is thermally stable (up to ~1550 K) and mechanically stable,[25] making it a potential desired inert support for Fe_2O_3 to form durable OCs in CLC, which, to our knowledge, has not yet been explored. In this study, two silicalite-1-supported Fe_2O_3 structures, (a) core−shell Fe_2O_3@silicalite-1 and (b) Fe_2O_3-impregnated silicalite-1 (Fe_2O_3/silicalite-1) were created for CLC and tested with methane fuel in a fixed-bed reactor. Fe_2O_3@silicalite-1 represents the silicalite-1 shell covered on the Fe_2O_3 core component[26,27] in the OC sample. The encapsulation of Fe_2O_3 inside the silicalite-1 shell or within its channels provides physical barriers for avoiding aggregations of OCs during CLC cycling, while the unique microporous structure of zeolite allows for transport of methane in and CO_2 out of Fe_2O_3 OC. An added benefit is that these structures reduce coke deposition on Fe_2O_3.

2. EXPERIMENTAL SECTION

2.1. Material Synthesis. *2.1.1. Preparation of Core−Shell Fe_2O_3@Silicalite-1 OCs.* Fe_2O_3 particles were prepared by dissolving 20.2 g of $Fe(NO_3)_3{\cdot}9H_2O$ (99.99% trace metal basis, Sigma-Aldrich) in 50 mL of deionized (DI) water under rigorous stirring, followed by the addition of 30 mL of KOH (⩾85%, Sigma-Aldrich) solution (5 mol L^{-1}) to form a $Fe(OH)_3$ suspension.[28] After adjusting pH of the suspension to ~10 by dropwise addition of NH_4OH solution (28.0−30.0%, Sigma-Aldrich), the mixture was stirred for 0.5 h, then transferred to a Teflon-lined stainless-steel autoclave, and held at 453 K for 5 h. Finally, the sample was then filtrated, washed with DI water and ethanol alternatively 4 times, and dried at 343 K for 12 h to form Fe_2O_3 particles.

Scheme 1 shows the procedure to prepare the Fe_2O_3@silicalite-1 core−shell structure with Fe_2O_3 as the core and silicalite-1 as the shell. First, a SiO_2 shell was created on Fe_2O_3 particles to form the core−shell Fe_2O_3@SiO_2 structure. In this synthesis, 0.1 g of as-synthesized Fe_2O_3 particles was first dispersed in a solution of 40 mL of 2-propanol (99.5%, Sigma-Aldrich), 1.42 g of DI water, and 1.1 g of NH_4OH solution (28.0−30.0%) by ultrasonication for 1 h. Second, a SiO_2 precursor solution was prepared by mixing 1 g of tetraethyl orthosilicate (TEOS, 98%, Sigma-Aldrich) with 2 mL of 2-propanol, and the resultant mixture was added to a Fe_2O_3 suspension at a rate of 0.4 mL h^{-1} via a syringe pump (NE-1000, New Era Pump System). After the mixture was stirred for 12 h, the resultant Fe_2O_3@SiO_2 particles were collected by centrifugation, washed with DI water 4 times, and then dried at 343 K overnight. Third, a vapor-phase transformation process was carried out to convert SiO_2 into silicalite-1 under assistance of silicalite-1 seeds to form the core−shell Fe_2O_3@silicalite-1 structure according to a previously reported method.[29,30] In this synthesis step, the as-prepared Fe_2O_3@SiO_2 particles were first dispersed in 4 mL of DI water by ultrasonication. A total of 2 g of poly(diallydimethylammonium chloride) (PDDA, 20 wt % in H_2O, Sigma-Aldrich) was mixed with 1 mL of DI water, and the resultant mixture was added to the Fe_2O_3@SiO_2 suspension. After the mixture was stirred for 0.5 h, the particles were centrifuged and washed with diluted NH_4OH (2 wt %) solution 4 times. The as-obtained wet paste was then dispersed in 10 mL of 1 wt % zeolite seed suspension for 0.67 h. The mixture was finally collected by centrifugation, washed with DI water 4 times, and then dried at 343 K overnight. The as-prepared Fe_2O_3@SiO_2 particles coated with PDDA and silicalite-1 seeds were transferred to a glass vial, which was placed in a Teflon-lined stainless-steel autoclave containing 2.0 g of trimethylamine (99%, Sigma-Aldrich), 0.2 g of ethylene diamine (99.5%, Sigma-Aldrich), and 0.4 mL of DI water.[30] The autoclave was heated at 413 K for 3 days to transform the amorphous SiO_2 shell into a silicalite-1 shell. Finally, the sample was calcined at 823 K for 4 h at a ramp rate of 1 K min^{-1} under flowing air (100 mL min^{-1}, Airgas). The Fe_2O_3@silicalite-1 sample was designated as Fe_2O_3@Si.

For the synthesis of silicalite-1 seeds,[29] typically, 0.43 g of NaOH (99%, Sigma-Aldrich) was dissolved in 15 mL of DI water, followed by the addition of 15 g of tetrapropylammonium hydroxide aqueous solution (TPAOH, 40 wt %, Alfa-Aesar) and 9.5 g of fumed silica (Sigma-Aldrich). The mixture was stirred at room temperature for 0.25 h and then heated at 353 K under stirring until a clear mixture was obtained. The resultant clear mixture was placed in a Teflon-lined stainless-steel autoclave, which was rotated at a speed of 30 rpm and under a temperature of 403 K for 8 h in a convection oven. Finally, the silicalite-1 nanoparticles were centrifuged, washed with DI water 4 times, and then dispersed in DI water to form 1 wt % silicalite-1 seed solution.

2.1.2. Preparation of the Fe_2O_3/Silicalite-1 Composite. Silicalite-1 zeolite was synthesized by a hydrothermal method using a recipe of 1TPAOH/8.5TEOS/0.17NaOH/34CH_3CH_2OH/484H_2O. In a typical synthesis, 0.032 g of NaOH was first dissolved in 20.2 g of DI water, followed by the addition of 1.22 g of TPAOH (40 wt %) aqueous solution. A total of 4.25 g of TEOS was added, and the resultant mixture was held under rigorous stirring at room temperature for 24 h. Finally, crystallization of silicalite-1 zeolite was conducted for 2 days in the autoclaves, tumbling vertically in an oven at 423 K. After crystallization, the zeolite product was centrifuged, washed with DI water until pH ~ 9, and dried at 343 K overnight. Afterward, the zeolite sample was calcined at 823 K for 6 h with a ramp rate at 1 K min^{-1} under flowing air (100 mL min^{-1}).

The synthesis of the Fe_2O_3/silicalite-1 composite was performed by an impregnation method. Typically, 0.35 g of $Fe(NO_3)_3$ was dissolved in 0.2 g of DI water, and the resultant aqueous solution was added to 1 g of silicalite-1 dropwise under rigorous stirring to form the 12 wt % Fe_2O_3/silicalite-1 sample. The process was repeated to make 24 wt % Fe_2O_3/silicalite-1, in which 0.70 g of $Fe(NO_3)_3$ was used. As-prepared 12 wt % Fe_2O_3/silicalite-1 and 24 wt % Fe_2O_3/silicalite-1 were dried at 393 K overnight, followed by calcination at 823 K for 4 h with a ramp rate of 1.67 K min^{-1} under air flow (100 mL min^{-1}). We designate 12 wt % Fe_2O_3/silicalite-1 and 24 wt % Fe_2O_3/silicalite-1 as Fe_2O_3/Si-12 and Fe_2O_3/Si-24, respectively, through the remainder of this paper.

2.2. Characterizations. The morphologies of the zeolite-supported Fe_2O_3 OC samples were characterized by scanning electron microscopy (SEM, Hitachi SU-70) and transmission electron microscopy (TEM, JEOL JEM 2100 FEG). The porosity, pore size, and surface area of these samples were obtained by argon (Ar) adsorption−desorption isotherms measured at 87 K with an Autosorb-iQ analyzer (Quantachrome Instruments). Crystal structures of OCs

DOI: 10.1021/acs.energyfuels.7b01689
Energy Fuels 2017, 31, 11225−11233

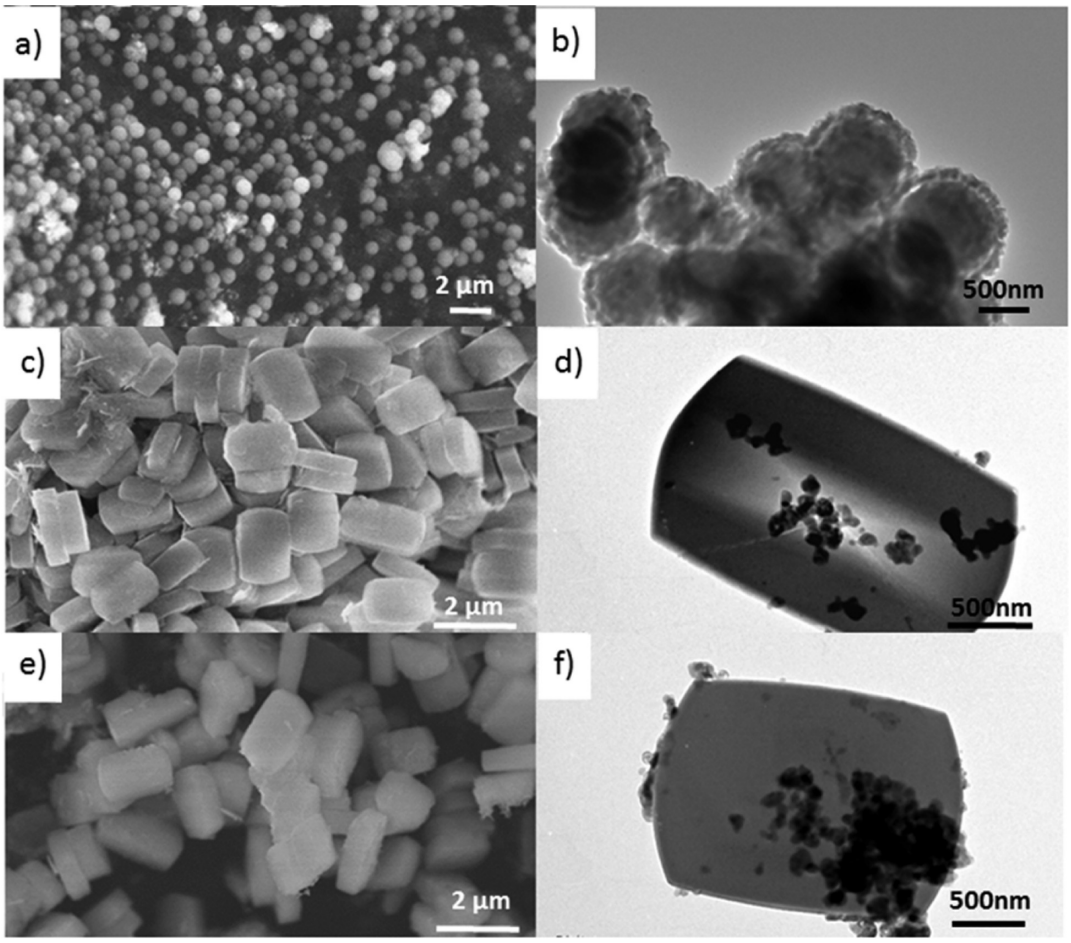

Figure 1. Morphology of OC samples viewed by SEM images of (a) Fe_2O_3@Si, (c) Fe_2O_3e/Si-12, and (e) Fe_2O_3/Si-24 and TEM images of (b) Fe_2O_3@Si, (d) Fe_2O_3/Si-12, and (f) Fe_2O_3/Si-24.

were characterized by X-ray diffraction (XRD) with a Bruker Smart1000 under a Cu Kα beam. Fe and Si contents of the samples were determined by inductively coupled plasma optical emission spectroscopy (ICP−OES, Optima 4300 DV instrument, PerkinElmer).

The cyclability and reactivity of OCs with CH_4 as fuel were carried out in a vertically oriented fixed-bed reactor in an electrically heated isothermal furnace, as reported in a previous publication.[14] Mass flow controllers (MFCs, MKS) regulated by a Labview VI program were used for gas reactant flow rate control. The reactor effluent was characterized by an online mass spectrometer (Stanford Research UGA 300) operating with a mass resolution of <0.5 atomic mass unit (amu), at 10% of the peak height and a detection limit of <1 ppm. Ar was used as an inert internal standard to determine the volume change of gaseous reactants and products during the reaction to assign concentrations. When the flow rates of CH_4 and O_2 were varied with a fixed Ar flow rate at 200 mL min^{-1}, calibrations for the mass spectrometer were obtained for CO_2, CO, CH_4, and H_2. About 200 mg of OC was used for each test, and for the supported OCs, samples containing this amount of Fe_2O_3 were used. The powders were packed within a quartz reactor tube of 610 mm length, with an outer diameter (OD) of 12.5 mm and inner diameter (ID) of 10 mm, as described in our previous work.[14] The particles were first annealed at 1023 K for 1 h and then exposed alternatively to 11% methane for 2 min and 20% oxygen for 5 min, simulating the CLC reaction cycles, with argon as the inert balance gas. Argon was introduced for 5 min during the shift from methane to oxygen to avoid direct contact between oxygen and methane. The CLC tests were run continuously for 50 cycles, at up to 15 h.

3. RESULTS AND DISCUSSION

3.1. Structural Properties of OCs. SEM and TEM images in Figure 1 show the morphologies of synthesized core−shell Fe_2O_3@Si and Fe_2O_3/Si composite OCs. Fe_2O_3@Si consists of uniform spherical particles of diameter at ∼1 μm (Figure 1a). The thickness of the silicalite-1 shell is ∼100 nm, and the Fe_2O_3 core has a diameter of ∼900 nm (Figure 1b). Panels c and e of Figure 1 are SEM images of Fe_2O_3/Si-12 and Fe_2O_3/Si-24, respectively, and both samples show a typical coffin-like morphology of silicalite-1, indicating that the loading of Fe_2O_3 and subsequent calcination did not change the morphology of the silicalite-1 support. Moreover, a comparison between the Fe_2O_3/Si-12 and Fe_2O_3/Si-24 samples, as evidenced by TEM images in panels d and f of Figure 1, indicates that there are more debris-like particle aggregates on silicalite-1 in Fe_2O_3/Si-24 than that in Fe_2O_3/Si-12, which can be attributed to the high loading of Fe_2O_3 in Fe_2O_3/Si-24.

The XRD patterns in Figure 2 identify the existence of both Fe_2O_3 and silicalite-1 crystalline phases in these three OC samples. For comparison purposes, the XRD patterns of silicalite-1 and Fe_2O_3 are included in Figure 2. Apparently, Fe_2O_3@Si contains the characteristic peaks of both hematite Fe_2O_3 (2θ = 33°, 35°, and 54°) and silicalite-1 (2θ = 23° and 24°), confirming the existence of silicalite-1 and Fe_2O_3 in this sample, consistent with morphology observation in Figure 1. XRD patterns of Fe_2O_3/Si-12 and Fe_2O_3/Si-24 in Figure 2 show the characteristic peaks of silicalite-1, consistent with the

DOI: 10.1021/acs.energyfuels.7b01689
Energy Fuels 2017, 31, 11225−11233

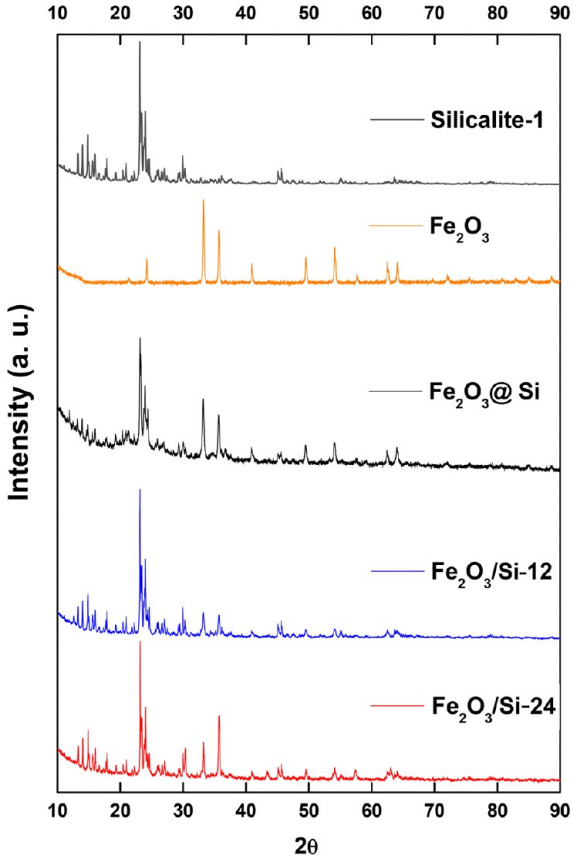

Figure 2. XRD patterns of silicalite-1, Fe_2O_3, and silicalite-1-supported Fe_2O_3 OCs.

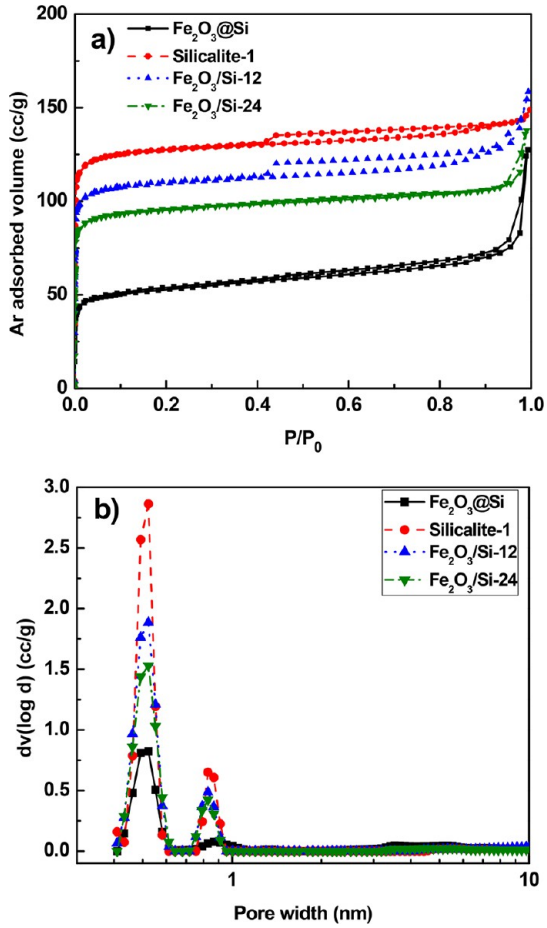

Figure 3. (a) Ar adsorption−desorption isotherms of OCs and (b) NLDFT pore size distributions of OCs derived from the adsorption branch of their Ar adsorption−desorption isotherms.

silicalite-1 crystal viewed in Figure 1. The intensity of diffraction peaks corresponding to Fe_2O_3 in Fe_2O_3/Si-12 is much smaller than that in Fe_2O_3/Si-24, which can be ascribed to the lower loading of Fe_2O_3 in the former sample.

3.2. Composition and Porosity of OCs. The concentrations of Fe_2O_3 in the OC samples were measured by ICP−OES, as summarized in Table 1. The weight percentages of Fe_2O_3 in Fe_2O_3/Si-12 and Fe_2O_3/Si-24 were 11 and 24 wt %, respectively, the same as the Fe_2O_3 concentrations used in the sample preparation recipe. The concentration of Fe_2O_3 in the Fe_2O_3@Si core−shell sample is 22 wt %, comparable to that in Fe_2O_3/Si-24.

Ar adsorption−desorption isotherms in Figure 3 are used to characterize the porosity of silicalite-1, Fe_2O_3/Si-12, Fe_2O_3/Si-24, and Fe_2O_3@Si samples. At the low relative pressure (p/p_0 < 0.05), the Ar uptake follows the order of Fe_2O_3/Si-24 < Fe_2O_3/Si-12 < silicalite-1, implying that the microporosity of silicalite-1 decreases with the increase of Fe_2O_3 loading. Fe_2O_3@Si (22 wt %) and Fe_2O_3/Si-24 (24 wt %) have similar Fe_2O_3 loadings, but the former sample has a much lower Ar uptake and, thus, microporosity. The low Ar uptake in the Fe_2O_3@Si sample might result from the existence of a portion of amorphous SiO_2 or not well crystallized zeolite in the silicalite-1 shell.

The pore size distributions of the OC samples are shown in Figure 3b, which are derived from the adsorption branch of the Ar adsorption−desorption isotherms using the non-local density functional theory (NLDFT) method.[31] The intensity of the micropore peaks, centered at ∼5 Å, shows the trend of silicalite-1 > Fe_2O_3/Si-12 > Fe_2O_3/Si-24, consistent with the Ar

Table 1. Composition Analysis of Fe_2O_3 in the OC Samples

material	density (g/cm^3)	percentage of Fe_2O_3 in OC samples[a] (wt %)	micropore volume of physical mixture[b] (mL/g)	micropore volume of OC samples[c] (mL/g)	percentage of Fe_2O_3 diffused into silicalite-1[d] (wt %)
silicalite-1	1.76[e]			0.128	
Fe_2O_3	5.24[f]			0.000	
Fe_2O_3/Si-12		11	0.114	0.103	52.0
Fe_2O_3/Si-24		24	0.097	0.086	24.6
Fe_2O_3@Si		22			

[a]Determined by ICP−OES. [b]Assumed that Fe_2O_3 is not diffused into silicalite-1 in Fe_2O_3/Si-12 and Fe_2O_3/Si-24. [c]Determined from Ar adsorption−desorption isotherm. [d]Fraction of Fe_2O_3 diffused into the micropores = [(1 − mass fraction of Fe_2O_3 in the OC) × micropore volume of silicalite-1 − micropore volume of the OC] × density of Fe_2O_3/mass of Fe_2O_3 in the OC. [e]Obtained from ref 25. [f]Obtained from International Chemical Safety Cards (ICSC), http://www.ilo.org/dyn/icsc/showcard.display?p_card_id=1577.

DOI: 10.1021/acs.energyfuels.7b01689
Energy Fuels 2017, 31, 11225−11233

Table 2. Reaction Equation in the Reduction Stage of CLC and Corresponding CO_2 Yield

	reaction equation	CO_2 yield (mmol/g of Fe_2O_3)
(1)	$\frac{1}{4}CH_4 + 3Fe_2O_3 \rightarrow 2Fe_3O_4 + \frac{1}{4}CO_2 + \frac{1}{2}H_2O$	0.52
(2)	$\frac{1}{4}CH_4 + Fe_2O_3 \rightarrow 2FeO + \frac{1}{4}CO_2 + \frac{1}{2}H_2O$	1.56
(3)	$\frac{3}{4}CH_4 + Fe_2O_3 \rightarrow 2Fe + \frac{3}{4}CO_2 + \frac{3}{2}H_2O$	4.69

isotherm data in Figure 3a, indicating that high Fe_2O_3 loading leads to more Fe_2O_3 diffused into the microporous channels of silicalite-1. The percentages of Fe_2O_3 diffused into the microporous channels of silicalite-1 in the Fe_2O_3/Si-12 and Fe_2O_3/Si-24 OC samples are 52.0 and 24.6% (Table 1), respectively. The Fe_2O_3@Si sample has the lowest micropore peak intensity, which might be due to amorphous SiO_2 or not well crystallized silicalite-1, as discussed above. The second peak located at 8 Å might be due to the reminiscence of a phase transition in Ar adsorbate according to previous reports.[32−34] The intensity of the mesopore peak in all OCs is very low, which suggests the absence of mesoporosity in these zeolite-supported OC samples.

3.3. OC Performance Tests in CLC. Table 2 lists the possible reactions occurring in the reduction stage of the CLC tests with Fe_2O_3 OCs and methane fuel. The CO_2 yield in each reaction is computed according to the equation stoichiometry.

Our measured CO_2 yield stabilized at 0.52 mmol/g of Fe_2O_3 for all OC samples at both 1023 and 1223 K for a 50-cycle CLC test, as shown in Figure 4. The CO_2 yield suggests that all OC samples give methane conversion preferentially following the first reaction equation in Table 2, which means that Fe_2O_3 is reduced into the Fe_3O_4 phase and is consistent with a previous report.[35] The XRD patterns in Figure 5 show the existence of Fe_3O_4 in the OC samples after the CLC test, which is consistent with the conclusion that Fe_2O_3 reduced to Fe_3O_4 in the CH_4 reduction step drawn from CO_2 yield data in Figure 4. The silicalite-1 support did not influence the reaction nature of Fe_2O_3 OCs in the CLC tests, consistent with the chemical and thermal inertness of silicalite-1 zeolite in the CLC conditions. In contrast to the independence of the CO_2 yield on the silicalite-1 support, the conversion rate of OCs in the CLC tests was influenced by the presence of the silicalite-1 support, as shown in Figure S1 of the Supporting Information. The OC conversion rates of three silicalite-1-supported Fe_2O_3 OCs are similar to each other but much faster than that of the bare Fe_2O_3 OC at both 1023 and 1223 K. This is due to the smaller Fe_2O_3 particles in the supported OCs because nanoporous silicalite-1 was effective in mitigating the sintering and/or agglomeration of these OC samples.

Because the primary motivation of developing the CLC process is for CO_2 sequestration, the exclusive formation of CO_2 versus other byproducts, such as coke (C), from methane fuel over OCs in the reaction is desired. In the present study, we did not observe any other gaseous carbon-based product, except CO_2, in the reduction stage of OCs. In the regeneration (or oxidation) stage of OCs, the CO_2 product was also observed, which results from the combustion of coke species deposited on OCs during the reduction stage in the CLC tests. Additionally, the H_2 product was detected in the reduction stage of OCs.

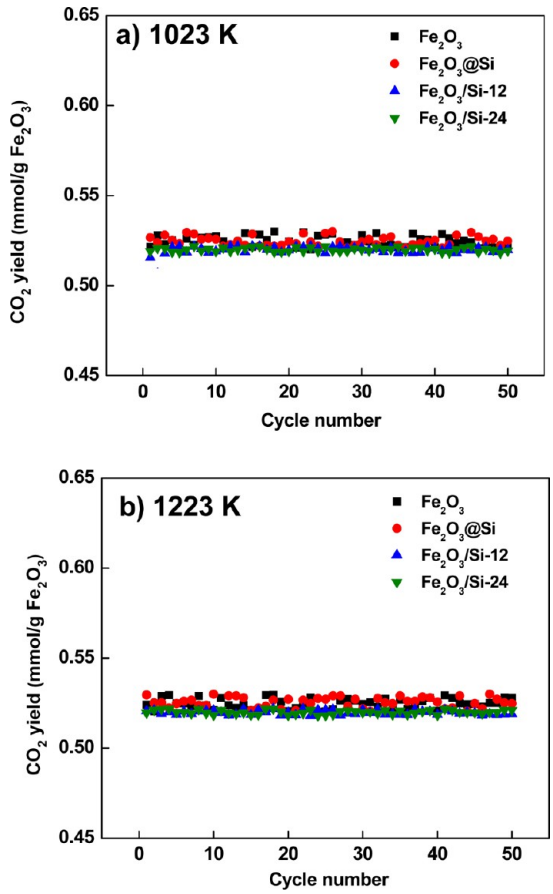

Figure 4. CO_2 yield in the CH_4 step at (a) 1023 K and (b) 1223 K of Fe_2O_3, Fe_2O_3@Si, Fe_2O_3/Si-12, and Fe_2O_3/Si-24 during the 50-cycle CLC reaction.

It is noted that two nominal side reactions, the Boudouard reaction (reaction 1) and the methane decomposition reaction (reaction 2), could occur in CLC of methane fuel.[36]

$$2CO \rightarrow C + CO_2 \quad (1)$$

$$CH_4 \rightarrow C + 2H_2 \quad (2)$$

The thermodynamic analysis shows that the methane decomposition reaction is endothermic while the Boudouard reaction is exothermic. Therefore, the methane decomposition reaction is thermodynamically preferred at high-temperature reaction conditions, while the Boudouard reaction is favored at low temperatures.[36] The absence of the CO product and presence of H_2 in the reduction stage of the CLC test indicate that methane decomposition is the side reaction in our study. Thus, the selectivity of CO_2 (γ_{CO_2}) is analyzed on the basis of the ratio of the CO_2 amount (n_{CO_2}) to total carbon-based species [i.e., the summation of n_{CO_2} and the amount of C (n_C)]

DOI: 10.1021/acs.energyfuels.7b01689
Energy Fuels 2017, 31, 11225−11233

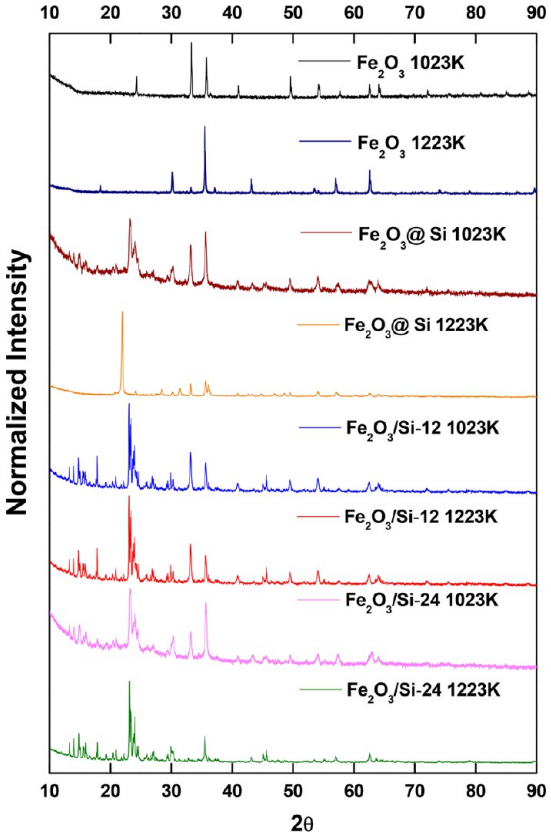

Figure 5. XRD patterns of Fe_2O_3 and silicalite-1-supported Fe_2O_3 OCs after the 50-cycle CLC reaction test.

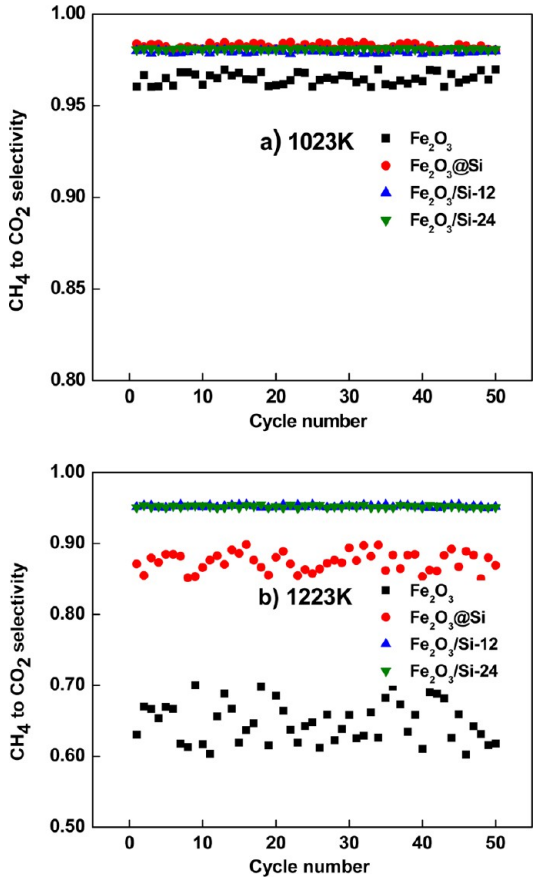

Figure 6. CH_4 to CO_2 selectivity, γ_{CO_2}, at (a) 1023 K and (b) 1223 K, respectively, over Fe_2O_3, Fe_2O_3@Si, Fe_2O_3/Si-12, and Fe_2O_3/Si-24 samples during the 50-cycle CLC reaction.

in the reduction stage, as shown in eq 3. It should be noted that coke generated from methane decomposition during the reduction step will subsequently be oxidized to CO_2 during the OC regeneration step (the O_2 oxidation step). The amount of coke was quantitied on the basis of the CO_2 emission from the oxidation step.

$$\gamma_{CO_2} = \frac{n_{CO_2}}{n_C + n_{CO_2}} \tag{3}$$

Figure 6 reveals CO_2 selectivity in CLC tests over Fe_2O_3 and silicalite-1-supported Fe_2O_3 OCs at two different tempreatures. At 1023 K (Figure 6a), all of the supported OCs (Fe_2O_3@Si, Fe_2O_3/Si-12, and Fe_2O_3/Si-24) showed similar CO_2 selectivity, ~97%, which was slightly higher than that of bare Fe_2O_3 OCs that had a CO_2 selectivity of ~95%. When the temperature was raised to 1223 K (Figure 6b), significant differences in CO_2 selectivity across these four OC samples were observed. The bare Fe_2O_3 OC only had a selectivity of ~65%. Fe_2O_3@Si had a better performance than bare Fe_2O_3, showing a selectivity of ~87%, but much less than Fe_2O_3/Si-12 and Fe_2O_3/Si-24 OCs. As shown in Figure 6b, both Fe_2O_3/Si-12 and Fe_2O_3/Si-24 had minimal performance degradation in the reduction stage, with a selectivity of ~95%. The slight differences in CO_2 selectivity at relatively lower temperature (1023 K) and significant differences at higher temperature (1223 K) across these four OC samples suggest that a higher reaction temperature may change the structures of the OC samples and, thus, alter their selectivity in the CLC reaction. The fluctuation in CO_2 selectivity for Fe_2O_3@Si and bare Fe_2O_3 samples might result from their morphology change in the CLC tests, as discussed below. Apparently, the Fe_2O_3-impregnated silicalite-1 samples have the best stability compared to others in the CLC tests.

To further understand the CO_2 selectivity at different temperatures over these OC samples discussed above, we monitored the temporal evolution of CO_2 and H_2 in the reduction step of the CLC process (shown in Figure 7). In the CO_2 evolution profile at 1023 K shown in Figure 7a, the CO_2 yield initially increased with the reduction time, reached a maximum, and then decreased. The peaking of the CO_2 signal for reaction over the silicalite-1-supported Fe_2O_3 OCs emerged earlier than the bare Fe_2O_3 OC sample. This is due to the large particle size of bare Fe_2O_3 without any zeolite support, which causes sluggish reaction kinetics compared to the reaction over smaller Fe_2O_3 particle sizes in the silicalite-1-supported Fe_2O_3 OCs.[14,17−20] At a higher reaction temperature (1223 K), the emergence of the maxima in the CO_2 evolution profile over every sample is earlier than that at 1023 K, suggesting that the reaction rate is facilitated as a result of the increase in the reaction temperature. Again, the peaking of the CO_2 signal for reaction over bare Fe_2O_3 lagged behind all other silicalite-1-supported Fe_2O_3 OCs. It should be noted that the CO_2 peak area resulting from reaction over every OC sample or every tested temperature is the same. This is consistent with the fact that the total yield of CO_2 was independent of the temperature or OC sample, as evidenced in Figure 5.

For the evolution profiles of H_2 in the CLC tests (shown in Figure 7b), all OCs showed nearly zero H_2 production at 1023 K, indicating the insignificant methane decomposition to form

DOI: 10.1021/acs.energyfuels.7b01689
Energy Fuels 2017, 31, 11225−11233

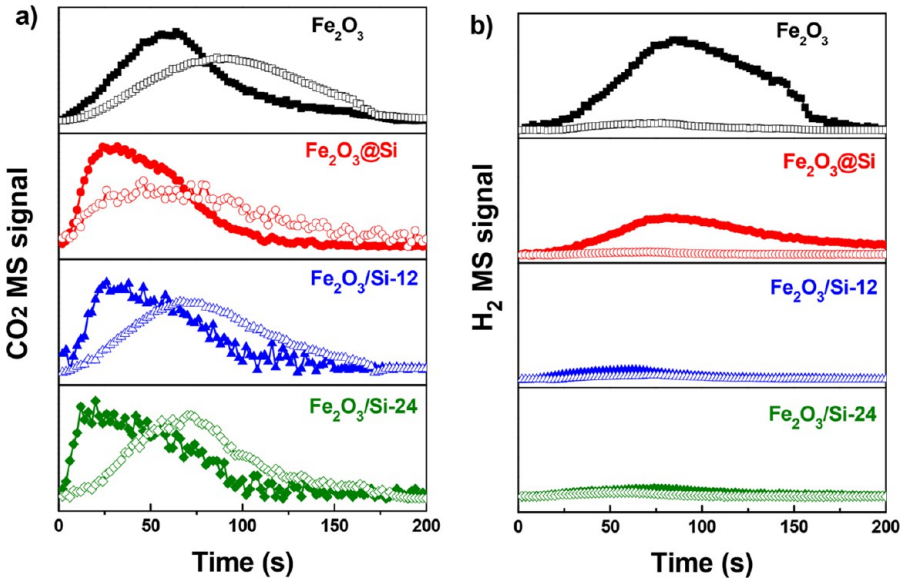

Figure 7. Evolution profile of (a) CO_2 and (b) H_2 in the reduction step during the 30th CLC cycle at 1023 K (open symbols) and 1223 K (filled symbols) for all OCs.

coke during the CLC reaction, consistent with the selectivity data presented in Figure 6a. At a reaction temperature of 1223 K, the H_2 evolution profile of bare Fe_2O_3 exhibited a pronounced H_2 peak, followed by the medium-sized peak from the Fe_2O_3@Si sample and invisible peak from Fe_2O_3/Si-12 and Fe_2O_3/Si-24. The emergence of the H_2 signal in the CLC tests indicates that coke was being formed from the methane decomposition reaction. Quite clearly, the resistance to coking in the CLC tests at 1223 K follows the sequence of Fe_2O_3/Si-24 ~ Fe_2O_3/Si-12 > Fe_2O_3@Si ≫ Fe_2O_3. This analysis fits well with the conclusion drawn from CO_2 selectivity data illustrated in Figure 6b. It is worth noting that H_2 production does not occur concurrently with CO_2 evolution and, instead, occurs behind the CO_2 formation. This scenario indicates that the side reaction, methane decomposition, is strongly promoted when labile framework oxygen in OCs is mostly consumed by the reduction of CH_4 to CO_2 at high temperatures. The zeolite support apparently helps the Fe_2O_3 OCs limit this side reaction and, thus, promote the CO_2 selectivity in the CLC process.

To examine the morphological structure of OCs after a high-temperature CLC reaction, SEM observation and XRD measurements were conducted on the used OC samples. Panels a, c, e and g of Figure 8 show SEM images of the four OC samples after 50-cycle CLC at 1023 K. In comparison to the morphology of silicalite-1-supported Fe_2O_3 samples before CLC tests (Figure 1), the Fe_2O_3@Si particles lost their smooth surface feature in the core−shell structure but still kept the spherical morphology. The Fe_2O_3/Si-12 and Fe_2O_3/Si-24 samples, however, have quite similar morphologies to those before CLC tests. The XRD patterns in Figure 5 confirmed the crystalline-phase integrity of four OCs after reaction at 1023 K, because all of them do not have new peaks in the diffraction patterns. These data confirm that all of the OCs can reserve their structural and chemical reactivity features at 1023 K in the CLC reactions.

Panels b, d, f and h of Figure 8 show the morphologies of all investigated OCs after 50-cycle CLC at 1223 K. Both unsupported Fe_2O_3 and Fe_2O_3@Si seem to be sintered together to form large aggregates (panels b and d of Figure 8, respectively). Particularly, the XRD patterns in Figure 5 indicate the transformation of silicalite-1 into amorphous SiO_2, consistent with the SEM observation on these two OC samples. The sintering of the silicalite-1 shell of the Fe_2O_3@Si particles might be due to the low structural crystallinity of the silicalite-1 shell (~100 nm thick), which is vulnerable and prone to collapse at high temperatures. Panels f and h of Figure 8 illustrate that Fe_2O_3/Si-12 and Fe_2O_3/Si-24 have little morphological change after 50 cycles of the CLC reaction at 1223 K. The XRD results in Figure 5 further confirm the presence of the silicalite-1 zeolite phase in the samples after CLC tests. In comparison to the thin silicalite-1 shell in Fe_2O_3@Si, the excellent structural stability of Fe_2O_3/silicailte-1 OCs should be ascribed to the large (~1 μm) and well-crystallized silicalite-1 crystals. Overall, the stable silicalite-1 zeolite provided physical barriers to avoid aggregation of active Fe_2O_3 OCs in CLC cycles, limited the coke deposition from the side methane decomposition reaction, and thus led to high CO_2 selectivity in CLC of methane fuel.

4. CONCLUSION

Silicalite-1 is explored as a novel support material for Fe_2O_3 to form supported OCs for the CLC reaction with methane as the fuel. Two silicalite-1-supported Fe_2O_3 structures, core−shell Fe_2O_3@silicalite-1 and Fe_2O_3-impregnated silicalite-1 (Fe_2O_3/silicalite-1), were created to study their influences on the CLC reaction at 1023 and 1223 K. After 50 cycles of CLC tests at 1023 K, both Fe_2O_3@silicalite-1 and Fe_2O_3/silicalite-1 OCs showed a similar CO_2 yield and slightly higher CO_2 selectivity than those of bare Fe_2O_3 OCs. All of the OC samples were able to preserve their structural integrity at 1023 K. An increase of the reaction temperature to 1223 K resulted in significant sintering of bare Fe_2O_3 and Fe_2O_3@silicalite-1 OCs, and thus, they showed inferior CO_2 selectivity than that of Fe_2O_3/silicalite-1 OCs. The larger silicalite-1 crystal in Fe_2O_3/silicalite-1 OCs keeps its structural integrity and provides physical barriers for Fe_2O_3 OCs against aggregation and coke deposition in CLC cycles. In conclusion, our study of the structure−function relation for silicalite-1-supported Fe_2O_3 OCs can form

DOI: 10.1021/acs.energyfuels.7b01689
Energy Fuels 2017, 31, 11225−11233

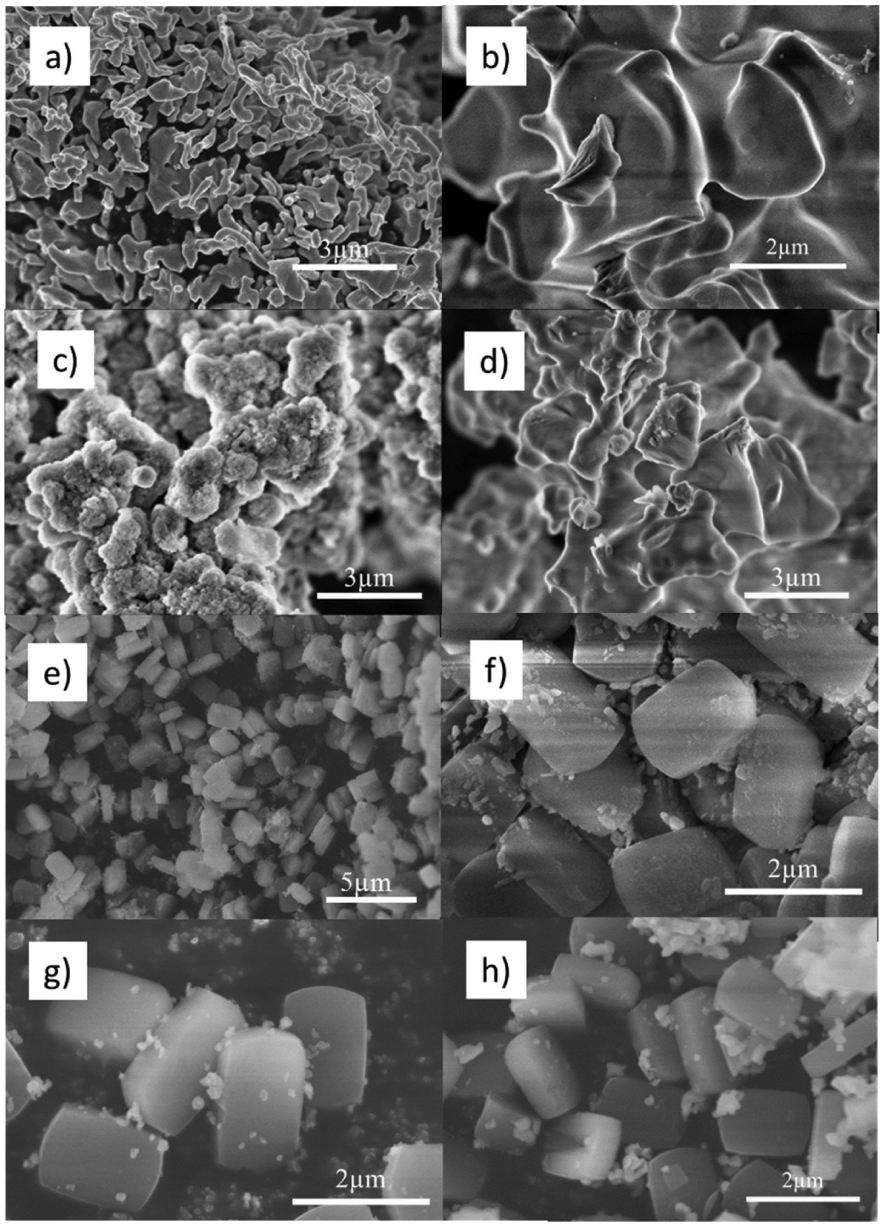

Figure 8. SEM images of the OCs: (a and b) Fe_2O_3, (c and d) Fe_2O_3@Si, (e and f) Fe_2O_3/Si-12, and (g and h) Fe_2O_3/Si-24 after the 50-cycle CLC reaction at 1023 and 1223 K, respectively.

the basis for the development of silicalite-1 as an efficient support in chemical looping applications.

■ ASSOCIATED CONTENT

Supporting Information

The Supporting Information is available free of charge on the ACS Publications website at DOI: 10.1021/acs.energyfuels.7b01689.

Conversion of OC in CLC tests (S1) and oxygen transfer capacity (S2) (PDF)

■ AUTHOR INFORMATION

Corresponding Authors

*Fax: +1-301-405-3522. E-mail: liud@umd.edu.
*Fax: +1-301-405-4311. E-mail: mrz@umd.edu.

ORCID

Michael R. Zachariah: 0000-0002-4115-3324

Author Contributions

†Lu Liu and Yiqing Wu contributed equally to this work.

Notes

The authors declare no competing financial interest.

■ ACKNOWLEDGMENTS

The authors thank the United States Department of Energy (DOE) and the National Science Foundation (NSF-CBET 1264599) for supporting this work. Yiqing Wu is thankful for the Hulka Energy Research Fellowship from the University of Maryland Energy Research Center (UMERC) to support his research.

■ REFERENCES

(1) National Research Council (NRC). *Advancing the Science of Climate Change*; The National Academies Press: Washington, D.C., 2010; pp 526.

DOI: 10.1021/acs.energyfuels.7b01689
Energy Fuels 2017, 31, 11225−11233

(2) Padurean, A.; Cormos, C.-C.; Agachi, P.-S. Pre-combustion carbon dioxide capture by gas−liquid absorption for Integrated Gasification Combined Cycle power plants. *Int. J. Greenhouse Gas Control* **2012**, *7*, 1−11.
(3) Liang, M. S.; Kang, W. K.; Xie, K. C. Comparison of reduction behavior of Fe_2O_3, ZnO and $ZnFe_2O_4$ by TPR technique. *J. Nat. Gas Chem.* **2009**, *18* (1), 110−113.
(4) Kanniche, M.; Gros-Bonnivard, R.; Jaud, P.; Valle-Marcos, J.; Amann, J.-M.; Bouallou, C. Pre-combustion, post-combustion and oxy-combustion in thermal power plant for CO_2 capture. *Appl. Therm. Eng.* **2010**, *30* (1), 53−62.
(5) Aleklett, K.; Höök, M.; Jakobsson, K.; Lardelli, M.; Snowden, S.; Söderbergh, B. The Peak of the Oil Age—Analyzing the world oil production Reference Scenario in World Energy Outlook 2008. *Energy Policy* **2010**, *38* (3), 1398−1414.
(6) Bolhàr-Nordenkampf, J.; Pröll, T.; Kolbitsch, P.; Hofbauer, H. Comprehensive Modeling Tool for Chemical Looping Based Processes. *Chem. Eng. Technol.* **2009**, *32* (3), 410−417.
(7) Richter, H. J.; Knoche, K. F. Reversibility of Combustion Processes. *Acs. Sym. Ser.* **1983**, *235*, 71−85.
(8) Ishida, M.; Zheng, D.; Akehata, T. Evaluation of a chemical-looping-combustion power-generation system by graphic exergy analysis. *Energy* **1987**, *12* (2), 147−154.
(9) Luo, S.; Zeng, L.; Fan, L. S. Chemical Looping Technology: Oxygen Carrier Characteristics. *Annu. Rev. Chem. Biomol. Eng.* **2015**, *6*, 53−75.
(10) Lyngfelt, A.; Leckner, B.; Mattisson, T. A fluidized-bed combustion process with inherent CO_2 separation; application of chemical-looping combustion. *Chem. Eng. Sci.* **2001**, *56* (10), 3101−3113.
(11) Liu, L.; Taylor, D. D.; Rodriguez, E. E.; Zachariah, M. R. Influence of transition metal electronegativity on the oxygen storage capacity of perovskite oxides. *Chem. Commun.* **2016**, *52* (68), 10369−10372.
(12) Cho, P.; Mattisson, T.; Lyngfelt, A. Comparison of iron-, nickel-, copper- and manganese-based oxygen carriers for chemical-looping combustion. *Fuel* **2004**, *83* (9), 1215−1225.
(13) Adanez, J.; Abad, A.; Garcia-Labiano, F.; Gayan, P.; de Diego, L. F. Progress in Chemical-Looping Combustion and Reforming Technologies. *Prog. Energy Combust. Sci.* **2012**, *38* (2), 215−282.
(14) Liu, L.; Zachariah, M. R. Enhanced Performance of Alkali Metal Doped Fe_2O_3 and Fe_2O_3/Al_2O_3 Composites As Oxygen Carrier Material in Chemical Looping Combustion. *Energy Fuels* **2013**, *27* (8), 4977−4983.
(15) Song, H.; Doroodchi, E.; Moghtaderi, B. Redox Characteristics of Fe−Ni/SiO_2 Bimetallic Oxygen Carriers in CO under Conditions Pertinent to Chemical Looping Combustion. *Energy Fuels* **2012**, *26* (1), 75−84.
(16) Mattisson, T.; Johansson, M.; Lyngfelt, A. Multicycle Reduction and Oxidation of Different Types of Iron Oxide Particles—Application to Chemical-Looping Combustion. *Energy Fuels* **2004**, *18* (3), 628−637.
(17) Arjmand, M.; Azad, A.-M.; Leion, H.; Lyngfelt, A.; Mattisson, T. Prospects of Al_2O_3 and $MgAl_2O_4$-Supported CuO Oxygen Carriers in Chemical-Looping Combustion (CLC) and Chemical-Looping with Oxygen Uncoupling (CLOU). *Energy Fuels* **2011**, *25* (11), 5493−5502.
(18) Zafar, Q.; Mattisson, T.; Gevert, B. Redox investigation of some oxides of transition-state metals Ni, Cu, Fe, and Mn supported on SiO_2 and $MgAl_2O_4$. *Energy Fuels* **2006**, *20* (1), 34−44.
(19) Johansson, M.; Mattisson, T.; Lyngfelt, A.; Abad, A. Using continuous and pulse experiments to compare two promising nickel-based oxygen carriers for use in chemical-looping technologies. *Fuel* **2008**, *87* (6), 988−1001.
(20) Li, F.; Sun, Z.; Luo, S.; Fan, L.-S. Ionic diffusion in the oxidation of iron-effect of support and its implications to chemical looping applications. *Energy Environ. Sci.* **2011**, *4* (3), 876−880.
(21) Johansson, M.; Mattisson, T.; Lyngfelt, A. Investigation of Mn_3O_4 With Stabilized ZrO_2 for Chemical-Looping Combustion. *Chem. Eng. Res. Des.* **2006**, *84* (9), 807−818.
(22) Galvita, V. V.; Poelman, H.; Bliznuk, V.; Detavernier, C.; Marin, G. B. CeO_2-Modified Fe_2O_3 for CO_2 Utilization via Chemical Looping. *Ind. Eng. Chem. Res.* **2013**, *52* (25), 8416−8426.
(23) Chen, Y. G.; Galinsky, N.; Wang, Z. R.; Li, F. X. Investigation of perovskite supported composite oxides, for chemical looping conversion of syngas. *Fuel* **2014**, *134*, 521−530.
(24) Kokotailo, G. T.; Lawton, S. L.; Olson, D. H.; Meier, W. M. Structure of Synthetic Zeolite ZSM-5. *Nature* **1978**, *272* (5652), 437−438.
(25) Flanigen, E. M.; Bennett, J. M.; Grose, R. W.; Cohen, J. P.; Patton, R. L.; Kirchner, R. M.; Smith, J. V. Silicalite, a New Hydrophobic Crystalline Silica Molecular-Sieve. *Nature* **1978**, *271* (5645), 512−516.
(26) Caruso, F. Nanoengineering of particle surfaces. *Adv. Mater.* **2001**, *13* (1), 11−22.
(27) Lou, X. W.; Archer, L. A.; Yang, Z. Hollow Micro-/Nanostructures: Synthesis and Applications. *Adv. Mater.* **2008**, *20* (21), 3987−4019.
(28) Huang, L. H.; Zhu, D.; Chen, Y. G.; Wu, C. L.; Sun, H. B.; Yang, H. Synthesis of monodisperse α-Fe_2O_3 deep-submicron spheres and its application in Li-ion batteries. *Mater. Lett.* **2012**, *74*, 37−39.
(29) Khan, E. A.; Hu, E. P.; Lai, Z. P. Preparation of metal oxide/zeolite core−shell nanostructures. *Microporous Mesoporous Mater.* **2009**, *118* (1−3), 210−217.
(30) Deng, Y. H.; Deng, C. H.; Qi, D. W.; Liu, C.; Liu, J.; Zhang, X. M.; Zhao, D. Y. Synthesis of Core/Shell Colloidal Magnetic Zeolite Microspheres for the Immobilization of Trypsin. *Adv. Mater.* **2009**, *21* (13), 1377−1382.
(31) Luisa Ojeda, M.; Marcos Esparza, J.; Campero, A.; Cordero, S.; Kornhauser, I.; Rojas, F. On comparing BJH and NLDFT pore-size distributions determined from N_2 sorption on SBA-15 substrata. *Phys. Chem. Chem. Phys.* **2003**, *5* (9), 1859−1866.
(32) Wu, Y. Q.; Emdadi, L.; Oh, S. C.; Sakbodin, M.; Liu, D. X. Spatial distribution and catalytic performance of metal-acid sites in Mo/MFI catalysts with tunable meso-/microporous lamellar zeolite structures. *J. Catal.* **2015**, *323*, 100−111.
(33) Thommes, M.; Mitchell, S.; Pérez-Ramírez, J. Surface and Pore Structure Assessment of Hierarchical MFI Zeolites by Advanced Water and Argon Sorption Studies. *J. Phys. Chem. C* **2012**, *116* (35), 18816−18823.
(34) Nakai, K.; Sonoda, J.; Yoshida, M.; Hakuman, M.; Naono, H. High resolution adsorption isotherms of N_2 and Ar for nonporous silicas and MFI zeolites. *Adsorption* **2007**, *13* (3), 351−356.
(35) Nasr, S.; Plucknett, K. P. Kinetics of Iron Ore Reduction by Methane for Chemical Looping Combustion. *Energy Fuels* **2014**, *28* (2), 1387−1395.
(36) Fan, L.-S. *Chemical Looping Systems for Fossil Energy Conversions*, 1st ed.; Wiley-AIChE: Hoboken, NJ, 2010.

DOI: 10.1021/acs.energyfuels.7b01689
Energy Fuels 2017, 31, 11225−11233